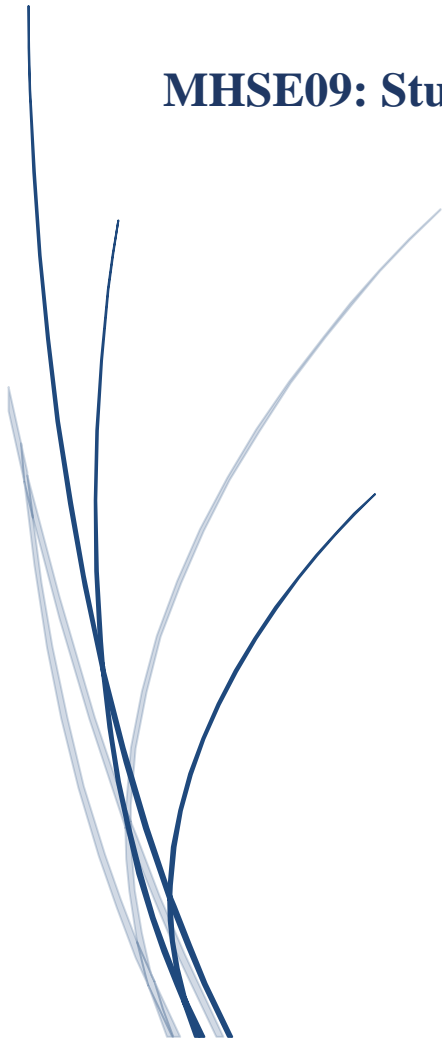TECHNISCHE
UNIVERSITÄT
DRESDEN

TECHNISCHE
UNIVERSITÄT
DRESDEN

Reanalysis of the 100-Year Flood in Wairau River Catchment

MHSE09: Study Project

Supervisor:
  Dr. Thomas Wöhling

Done by:
  Adeyemi Adejare   4980429
  Jagan Kuppusamy   4992159
  Nandhini Suthesh   4992040

List of contents

List of figures

List of tables

Used abbreviations

MDC – Marlborough district council

RBF – Radial Basis Functions

NN – Natural Neighbour

IDW – Inverse Direct Weighting

EBK – Empirical Bayesian Kriging

NIWA - National Institute of Water and Atmospheric Research

CCF – Cross-correlation Function

1. Introduction

The need for water resources for agricultural, municipal usage, industry, and energy production has steadily increased in these modern days of industrialization. The concerns over the long-term yield and nutrient contamination have prompted a number of hydrological research on the Wairau aquifer over time in order to better understand the surface-groundwater interaction (Morgenstern, Davidson, et al., 2019). The Wairau River has experienced significant hydrological changes in recent decades, owing to a variety of variables including climate change, environmental changes, and engineering projects. As a result of the recent development of a restricted floodway river, the river has been trained into a constrained and channelized form. The river's effective width has diminished as a result of the training, limiting the volume of water restored into the Wairau aquifer.

The Wairau River, one of New Zealand's most important rivers, provides a major source of irrigation and water supply for the Marlborough residential region. New Zealand's wine industry is the world's sixth-largest, with the Marlborough region accounting for roughly 70% of all exports. For the past 130 years, a number of river protection systems have been implemented in the Wairau region to channel floodwaters and safeguard the region from flooding. Unfortunately, due to extraordinary extreme events like the 1983 flood event, which resulted in an initial peak discharge of 7000 m^3/s, a 1 in 150-year return period event, the pre-constructed flood control systems in the Wairau River and its tributaries have failed to safeguard the flood plains. After this incident, several protection measures were implemented, and it was regarded as the most extreme event before the 2021 flood disaster. With a 100-year return period, the July 2021 flood event delivered a peak flow of 6000 m^3/s. With up to 291mm of rainfall in a 24-hour period and hourly intensities of up to 25 mm per hour, the principal rainfall event was centered on the Richmond Range. This research focuses on the July 2021 floods, which caused massive economic damages, particularly in the wine industry. To overcome the difficulties posed by extreme flood events, a thorough analysis must be conducted to gain a better understanding of the flood behavior.

The purpose of this study is to access the possibility of a good estimate over the areal precipitation data for flood forecast and rainfall model recommendation also, to investigate the surface-groundwater interaction during the flood. The objectives are to estimate the flood event parameters, interpolate, and explore the sensitivity of each approach for catchment precipitation, and finally analyze groundwater response data.

2. Literature review

Reanalysis efforts are continuously undertaken at major numerical weather prediction centres and meteorological research institutes. It is essential to improve the quality and availability of observational datasets for further advances in reanalysis. Several international activities are retrieving historical observations and reprocessing satellite observations. (S. Kobayashi, 2015)

Though floods caused by heavy rains are predictable, the accuracy is dependent on the degree of predictability of precipitation. The severity of the flood is understood by studying the river flow data. (L.M. Korytny, 2006)

Rivers that flow all around the year are most likely provided by groundwater. The existing baseflow in the river could be found by the hydrograph separation method. (I. Mondal, 2016)

The separation of streamflow hydrographs into rapid streamflow and baseflow is done to understand the processes of a watershed. Topography differences can vary the infiltration rate and influence the transport of streamflow. The graphical method like the straight-line method to separate the baseflow is well suitable for a single storm event. (D.D. Bosch, 2017)

The relationship between flow and precipitation is widely studied by the calculation of total areal precipitation. Also, the size and shape of the catchment could affect the total volume of flow in the stream and the shape of the hydrograph. (S. Ogras, 2020)

The magnitude of flood also depends upon the antecedent hydrological processes over many preceding timescales. Antecedent moisture conditions can have an elevated influence on the flood event besides the high precipitation occurrence. (B. Bennett, 2018)

Choosing an appropriate interpolator is essential to have reliable assessments. Cross-validation and split-sample validation methods were reliable (Y. Wu, 2019). Having the data from meteorological stations, the unknown values of a surface are predicted by spatial interpolation. Generally, no interpolation method is better than the other. The smoothness of the data throughout the area produces better interpolation. (S.J. Hadi, 2018)

From a previous study, the performance of the interpolation techniques depends upon the sample density, climatological characteristics, and topography (R. Yang, 2021). Understanding the spatial

variability related to the geological and geophysical information represents the true heterogeneity present in the study area (E. Gringarten, 2001).

The spatial pattern and the amount of precipitation are dependent on the orography. Areas with sparsely available measuring stations might require representation in relation to elevation and other topographical parameters. The different areal precipitation estimates are tested by comparing observed discharge and discharge simulated by a hydrological model with different estimated precipitation. Though precipitation data sets are different with respect to the spatial distribution, the precipitation data sets proved to have relatively high values along the mountains and relatively lower values along the valley. (D. Duethmann, 2012)

The dynamic recharge rates of the river are affected by the frequency and duration of the low-flow periods and a reduction in connectivity of the river and aquifer. The aquifer storage cannot be refilled during a single extreme flood event due to the upper threshold for exchange flows (T. Wöhling, 2018)

Rainwater recharge happens rapidly in mountainous areas with thinner soil and with shallow unsaturated depths. The contrasting lag time of the maximum correlation between rainfall and groundwater level change gives an understanding of natural groundwater recharge which functions with the help of factors like topography and soil thickness. (G. Chae, 2016)

The peak lag time of the groundwater monitoring wells with the flood increases with an increase in distance from the banks of the river. The flood arrived three to four times slower to the wells away from the banks. (A. Hervai, 2020)

3. Methods

3.1. Study area

The Wairau River is located in Marlborough, a region in the northeast of the South Island of New Zealand. It is the largest river in Marlborough and the sixteenth longest river in New Zealand, with a length of 170 km and a catchment area of 3,430 square kilometres, occupying up to one-third of the land area in that region (Wöhling et al., 2020). The river flows from south to north, beginning in the Spencer Mountains at an altitude of 2,202 meters, after which it flows north-west through the alpine fault-filled by glacial outwash before entering the sea at Wairau Bar into Cloud Bay at

the end of its course. The runoff regime of the river Wairau is volatile, with an average yearly flow of 100 m³/s and the highest flow reaching up to 1950 m³/s. Its tributaries include the Rainbow River, Marchburn River, Goulter River, Waihopai River, Tuamarina River, among others (Cookson, 2020). At the end of the river, there are lagoons and salt marshes that serve as wildlife habitats.
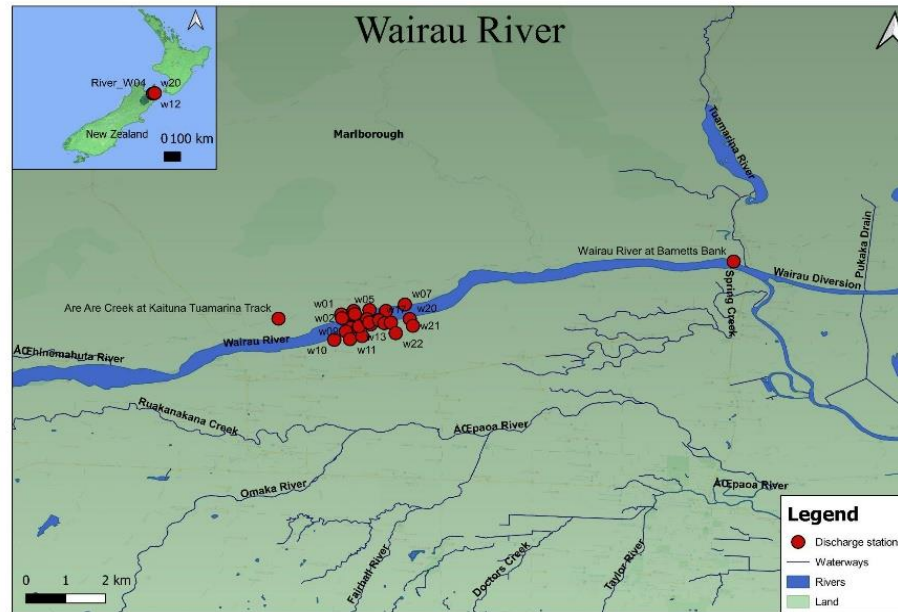
Figure 1: Study area with discharge stations.

3.1.1. Climate

The catchment area of the Wairau River is characterized by a wet climate with a mean annual precipitation of 650mm near the coastline and up to 2500 mm in the mountain regions to the north and west (Wöhling et al., 2020). It is a warm region, with its vegetation being mainly native forest. The catchment is also known for its high-intensity thunderstorms that occur on average five to ten times annually (Simpson et al., 1980).

Summer afternoons in the Wairau valleys and lowlands are warm with temperatures above 22°C. Higher elevation areas have cooler summer afternoon temperatures ranging between 16°C and 21°C. Winter, on the other hand, in elevated areas has a daily temperature of between 6°C and 8°C, while lowland areas span between 1°C and 4°C. On the median annual temperature, however, the temperature is about 12.5°C on the lowlands and 8°C to 11°C in higher elevation areas (Chappell, 2016).

3.1.2. Geomorphology

The Wairau River consists of impermeable basement rocks and permeable gravel. The active Wairau and Alpine Faults intersect the catchment and divide major basement rock sections into northern and southern sub-catchments. To the north, the basement rocks majorly include sedimentary and igneous rocks that have become metamorphosed into Permian rocks (schists). The south consists primarily of greywacke (Cretaceous and Triassic sandstone) and argillite with minor overlying Tertiary sediments (Morgenstern et al., 2019). Near the coastal lines is late Pliocene to early Pleistocene Hillersden tight gravels and tertiary rocks that overlie basement greywacke. Pleistocene and Holocene gravels, also referred to as Rapaura gravels, stated to be 20 m to 30 m thick, are also found in the Wairau Valley and merge with the Dillons Point formation that consists of swamp deposits and fine-grained estuarine (Taylor et al., 1992). Underneath the Holocene gravels of the Rapaura formation lies the Speargrass formation, which is orders of magnitude less permeable and thus considered to be a confining unit (Christensen and Doscher, 2010).
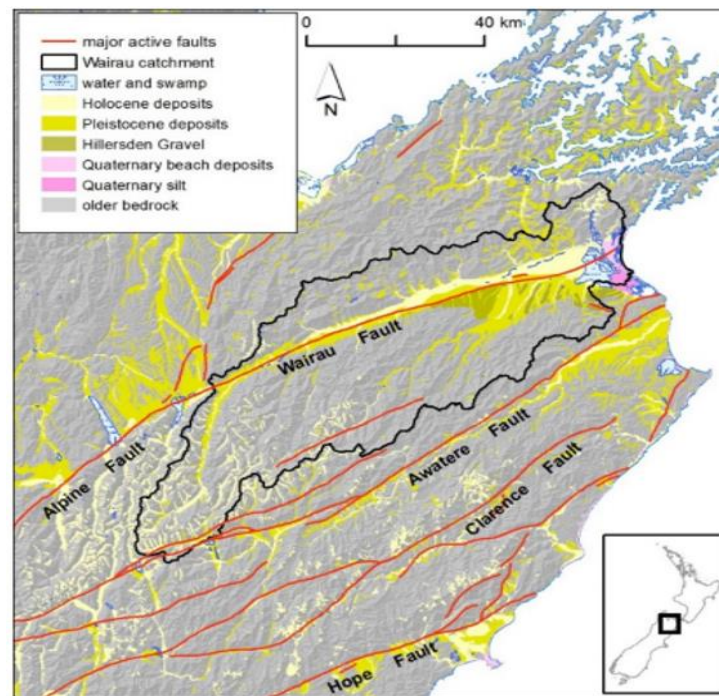
Figure 2: Basic geology of the Wairau River catchment area (Morgenstern et al, 2019).

3.2. Data used

The data used for this research were observed by the Marlborough District Council (MDC). However, there was a loss of data during the flood event.

Table 1: Data used in the study

Station Coordinates	• Discharge
	• Precipitation
	• Monitoring wells
Discharge [m³/s]	• Are Are Creek at Kaituna Tuamarina Track
	• Barnetts Bank
	11.08.2020 to 30.09.2021 at 15 minutes interval
Temperature [º C] & Piezometric Heads [m]	Water Table in the Wairau Catchment
Precipitation [mm]	• Aggregated Precipitation
	15.07.202118.07.2021
	• Rain RADAR Data
	16.07.2021 to 20.07.2021

3.3. Measurement stations

The discharge and precipitation coordinates with the catchment outline were overlaid onto the Marlborough shapefile to visualize the distributions of the measurement sites over the Wairau River. The precipitation stations are spatially distributed over the Wairau River with some stations located outside the catchment. The Barnetts Bank is the main catchment outlet downstream, while the Are Are Creek upstream is one of the tributaries to the Wairau River (Figure 1). The Creek is important and considered because it may influence the groundwater levels at the study site.
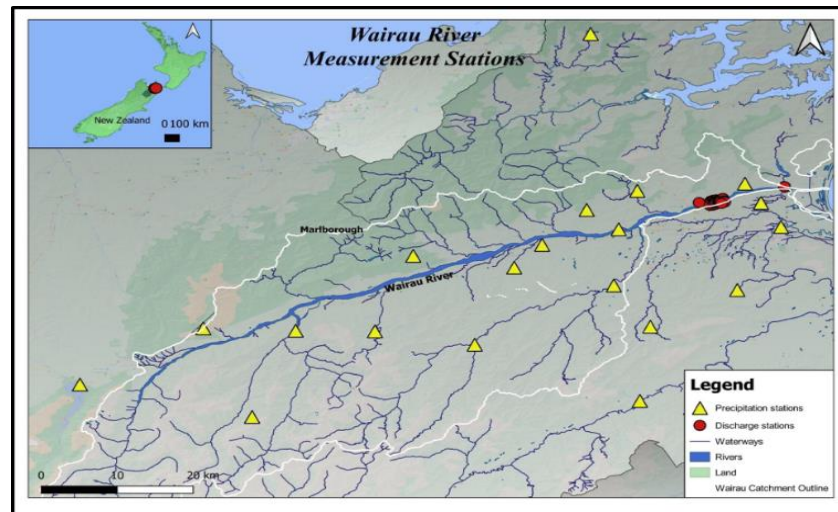
Figure 3: Precipitation and Discharge stations along the Wairau River, New Zealand.

3.4. Flood hydrograph

The discharge was plotted against time to observe and estimate the flow volume during the event. The peak flow is contained in the crest segment that extends from the point of inflection on the rising limb to another point of inflection on the falling limb. The crest segment has the highest concentration of the total volume of the flood event and consists of the maximum streamflow discharge values. The peak discharge at two stations: Barnetts and Are Are Creek was estimated at 6037.849 m³/s and 121.69 m³/s respectively. This peak was on the afternoon of July 17, 2021. The recession limb which starts at the inflection point in the falling side happened two days after the peak and this represents the withdrawal of water from various storages in the catchment as well as deposition into the sea. The shape of the recession limb depends on the characteristics of the catchment. A few days before the beginning of the main flood event, the streamflow had increased and had a maximum of 342 m³/s at Barnetts station. There also exists another small surcharge just after the flood event, which could be due to the late discharge from the catchment into the river at Barnetts station.

Figure 4: Flood Hydrograph at Wairau River from 02-28th July 2021 (Barnetts Bank and Are Are Creek).

3.4.1. Baseflow separation

The existing flow in the river apart from the flood events throughout the year is called a baseflow. Calculating the baseflow is vital in understanding the hydrology of a watershed. The baseflow which is included in the flood event was removed to know the exact flood volume for further

analysis. For individual storm events, the hydrograph separation method of the straight-line method is widely used also in this study.
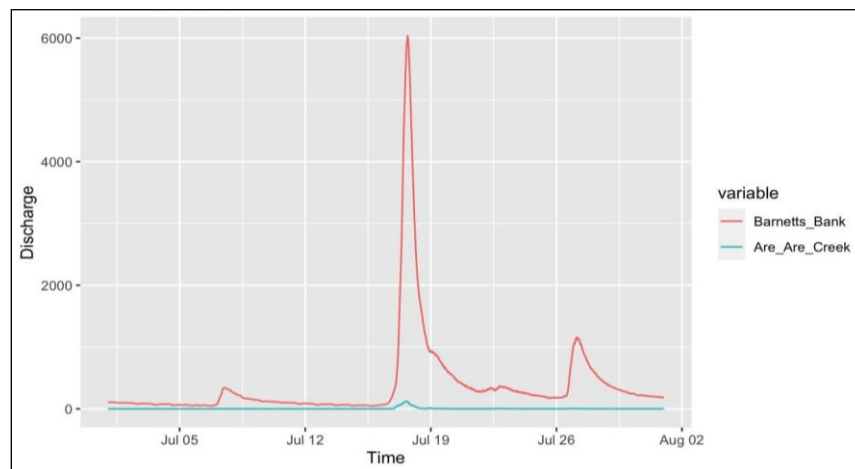
The starting point of the straight line is where there exists a sudden increase in streamflow and until this point, streamflow is equal to baseflow and after the end of direct runoff. This starting point is where the direct runoff starts and the hydrograph rises at a significantly faster rate compared to the previous values. This can be found by visually inspecting the data after plotting. Direct runoff is the difference between streamflow and baseflow. The straight line ends at the end of the falling limb of the hydrograph. The figure 5 below shows the straight line which was used in separating the direct runoff from the total runoff in the study.
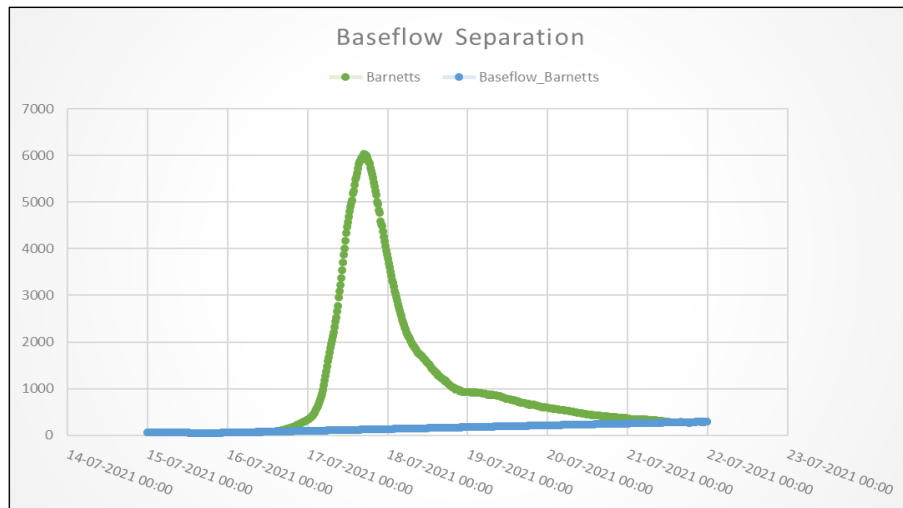
Figure 5: Baseflow separation of the streamflow at Barnetts station

3.4.2. Flood Volume estimation

After the separation of the baseflow, the data was inputted along with the discharge, net-flow, and timesteps to obtain the flood volume. The net-flow was calculated by separating the baseflow from discharge for the entire flow data as shown in equation 1:

$$Q_{\text{Net-flow}} = Q_{\text{Barnets}} - Q_{\text{baseflow}} \qquad \text{……….. Equation 1}$$

where,

$Q_{\text{Net-flow}}$ – resultant of discharge at Barnets and baseflow

Q_{Barnets} – discharge at the Barnetts

Q_{Baseflow} – flow obtained after separating baseflow.

Then, the result obtained from the data after baseflow separation was multiplied with the difference of each interval for corresponding data. This data was further summed up to obtain the flood

volume for the entire July event. Further, the areal precipitation was calculated by dividing the flood volume by the catchment area.

3.5. Spatial interpolation

3.5.1. Geostatistical Interpolation

The observed aggregated precipitation data was merged with the location coordinates and interpolated using different interpolation techniques to observe the plausibility of the patterns that arise and evaluate the differences in the areal catchment precipitation for the selected methods. Four geostatistical interpolation methods were selected, namely: Radial Basis Functions (RBF), Natural Neighbour (NN), Inverse Direct Weighting (IDW), and Empirical Bayesian Kriging (EBK) interpolation. The output of the individual interpolation methods was converted to a raster map, and the raster cells within the catchment were averaged.

The rain RADAR data for the July 2021 flood event was collected from the Marlborough District Council and the National Institute of Water and Atmospheric Research (MDC/NIWA). The data were aggregated, analyzed, and plotted for the period from 16-Jul-2021 to 20-Jul-2021. This was used to compare the results from the interpolation schemes.

3.5.2. Variogram

The variogram is a widely used tool for quantifying the spatial variability of spatial phenomena. The experimental variogram is a discrete function computed using a measure of variability between pairs of points separated by different distances. The precise measurement depends on the variogram type chosen (Deutsch and Journel, 1997). In this research, the exponential (exp) and spherical (shp) models were selected as they fitted best for the data type to investigate and quantify the spatial correlation of the precipitation measurements. The precipitation sums from the individual 22 precipitation stations were collected and interpolated.

The x-axis shows the distance between two stations, while the y-axis shows the semivariance, which is a measure of similarity between two points (Fig 5). With 22 stations and combinations of 2 stations, there are a total of 231 points in the variogram. We use bins of different distance ranges to detect spatial structure and compute semivariance for all points in the individual bins. The bin sizes for each of the selected models were varied using width sizes of 1000 m, 2000 m, and an autofit model to obtain different experimental variograms. The spatial structures of the map were

later plotted to evaluate the average precipitation of each model type. The interpolation was achieved by using the ordinary kriging method. Its purpose is to estimate a value at a point in a region where a variogram is known by using the neighbourhood data of the estimation location.

Ordinary Kriging can be expressed as $Z(s) = m(s) + e(s)$ ……… Equation 2

Where $Z(s)$ is the attribute value at the spatial position s, $e(s)$ is the autocorrelated error term which depends on the spatial position s, while the trend depends on the spatial location of the observation $m(s)$.

(a): Variogram 1   *(b): Variogram 2*
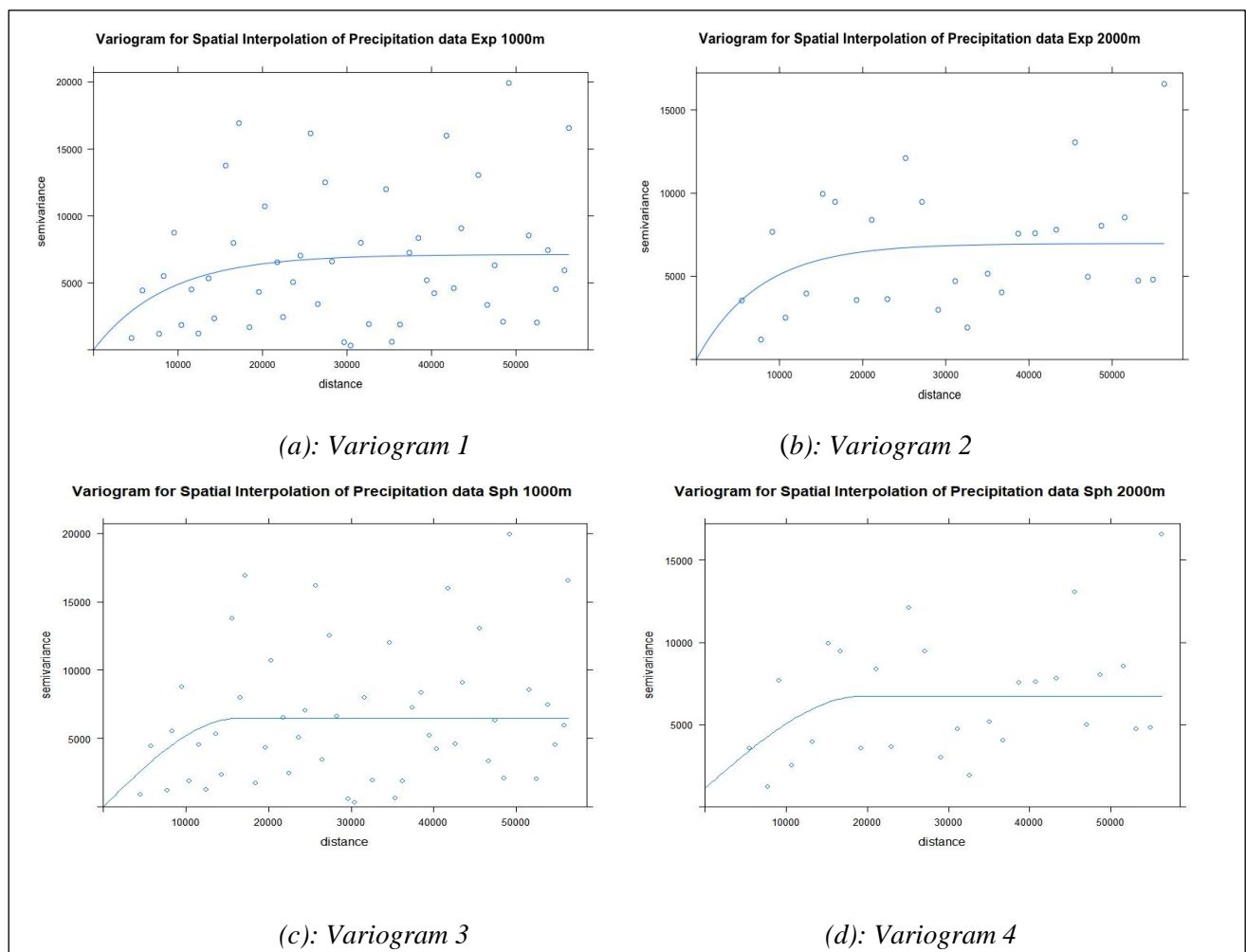
(c): Variogram 3   *(d): Variogram 4*

Figure 6: Variogram for precipitation data using Exponential and Spherical models with varied bin sizes of 1000 m and 2000 m.

a). sill=7125, range=8642, nugget=0, width=1000 m, model=Exp

b). sill=6971, range=7581, nugget=0, width=2000 m, model=Exp

c). sill=6459, range=16295, nugget=3.8, width=1000 m, model=Sph

d). sill=5617, range=19607, nugget=1127, width=2000 m, model=Sph

3.6. Groundwater Analysis

3.6.1. Groundwater Flow

Groundwater is usually contained within impermeable layers called aquifers and when the geology changes making the water move through the soil strata. As a part of the hydrological cycle and the gradient as well, this groundwater moves into the streamflow when the geology favours the connectivity of the aquifer with the river. And this groundwater flow also contributes to the baseflow of the river.

Intense precipitation over catchments causes infiltration which leads to an increase in the water table of the aquifers. Surface water flooding happens in the case where the water table is in an already saturated state and the precipitation prolongs. Usually, when there is no flood, the groundwater flows from high gradient regions to the lower ones towards the river and during the flood, it flows in the opposite direction. To understand the flow of groundwater over a region, the development of contour maps is done. The monitoring wells spread over the area, collected data of piezometric head and temperature were further used for creating contour maps.

3.6.2. Contour maps

Contour maps especially for water levels are typically used to understand the flow in the space and this could indicate the continuity and the obstruction. The relationship between the water in the aquifer and the one on the surface could also be understood with contour maps. Contour maps of water level and temperature were considered in this study.

Taking the monitoring wells from the water table and the measuring stations from the river into consideration, contour maps were generated by spatial interpolation using the ordinary Kriging method. The contour maps were generated for the periods before, during, and after the flood event. Following the same method, the difference in values in-between periods was depicted as fluctuation maps for further understanding in the study. Perpendicular to the contour lines of decreasing magnitude would indicate a flow of water in that direction.

3.6.3. Timeseries analysis

Timeseries were plotted for the stage and temperature to visualize the continuity of the data. The data was aggregated for the duration of the flood, and each of the data from the corresponding wells was plotted to check for outliers.
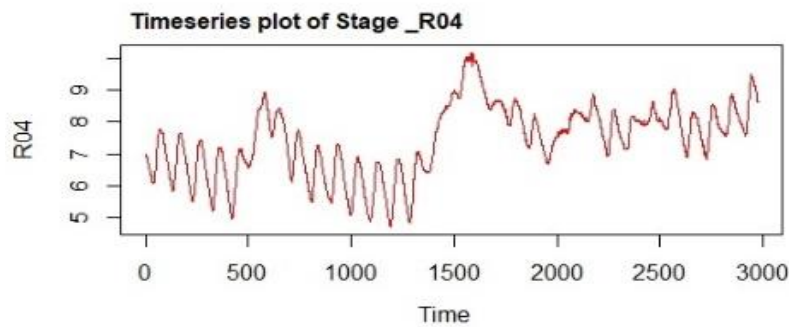

Figure 7: Timeseries plot of R04 against Time.

Figure 7 shows an example of the timeseries plotted for the stage of the river station R04. Similar to the plots as shown in figure 7, the timeseries were plotted for all the stage and monitoring wells and visually inspected for outliers. The application of timeseries gives a better understanding of the seasonality and trend, which further leads to linear regression modelling.

3.6.4. Detrending the timeseries

 Before performing the correlation analysis, the temperature data were detrended to remove the seasonality in the data. After plotting the timeseries for Stage and temperature for both water level and temperature it can been seen that the water level had a good temporal variation and thus the detrending is only concentrated on Temperature data which has a very high seasonality in the trends.

The linear trends and seasonality were removed to fit the model into linear regression and removing the trend from the model. Figure 8 shows the timeseries plots of Well_W01 before and after detrending. The trends were removed for all the stage and groundwater wells and these data was further used for cross-correlation. This gives us the scope to understand the correlation of temperature between groundwater and water level of the river.
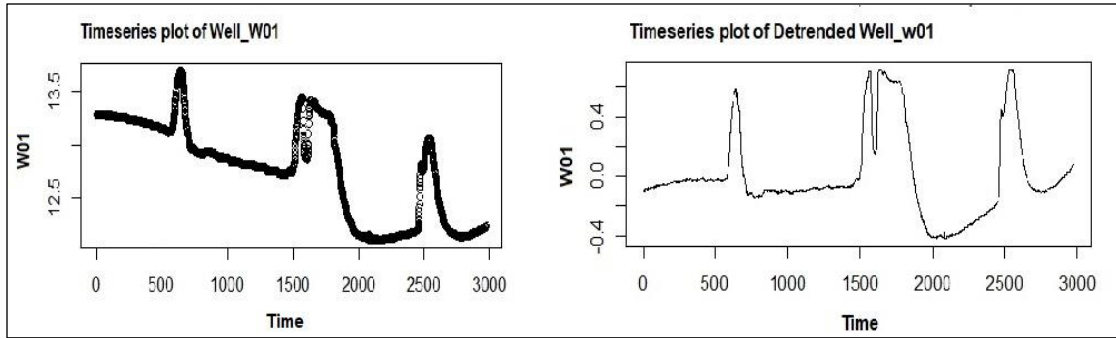
Figure 8: Plots of Timeseries of Well_W01 before and after detrending.

3.6.5. Cross-correlation

The technique of cross-correlation analysis is commonly used in the study of interactions between groundwater systems and their boundary conditions, such as recharge from precipitation or discharge from rivers, lakes, streams, or springs (Kristijan Posavec, Perica Vukojevi, 2015). Cross-correlation is a measure of similarity between two series (i.e., the degree to which two series are linked with respect to the lag of one relative to the other) and the process of comparing them at consecutive lags. This study employed cross-correlation to examine the temporal dependency of water level and temperature between river and groundwater, which gives a better understanding of the river-groundwater interaction.

Timeseries were compared with each other with their sequential lags to calculate the position of the river and groundwater level. The time lag between the river stage and groundwater determines the point of maximum equivalency, which is used to compute the groundwater pressure transit time. The measured groundwater and river stage are acquired at the same time and date as the cross-correlation analysis of the time series for the appropriate lag times. The alignment of two series at their origins is compared at their consecutive delays using the zeroth lag.

The strength of cross-correlation between the timeseries is determined using the relation given in equation 3 as follows:

$$r_m = \frac{n\sum Y_1 Y_2 - \sum Y_1 \sum Y_2}{\sqrt{\left[n\sum Y_1^2 - \left(\sum Y_1\right)^2\right]\left[n\sum Y_2^2 - \left(\sum Y_2\right)^2\right]}} \quad \text{…. Equation 3}$$

Where,

> r_m – correlation coefficient for each match position m,

> n – the number of overlapped positions between the two timeseries,

> Y1 and Y2 – two timeseries being compared

Equation 3 only applied to overlapped segments of the two timeseries being compared, the absolute maximum number of overlapped locations n between the two series equals n*-2, where n is the total number of data points in the given time series. In general, the cross-correlation algorithm examines two time series at successive lags, calculates the correlation coefficients, and plots the maximum equivalency r Lag max is the lag referred from zeroth lag and represents the greatest correlation coefficient for all overlapping points between the two-time series.

4. Results

4.1. Flood volume hydrograph

After determining the baseflow components at each timestep for Barnetts, the net-flow was calculated by identifying the difference of the discharge and Baseflow at the Barnetts. The flood volume was then determined by the product of the net-flow and frequency of each time step (15 minutes interval). The total flood volume was resulted by summing up the volume at each time step and was resulted to be 5.1×10^8 m^3. Furthermore, the areal precipitation for the total flood volume was estimated to 148.68 mm by dividing the total volume by catchment area which is 3.43×10^6 m^2. The figure 8. shows the flood volume hydrograph. The graph was plotted with time in x -axis and discharge in y- axis
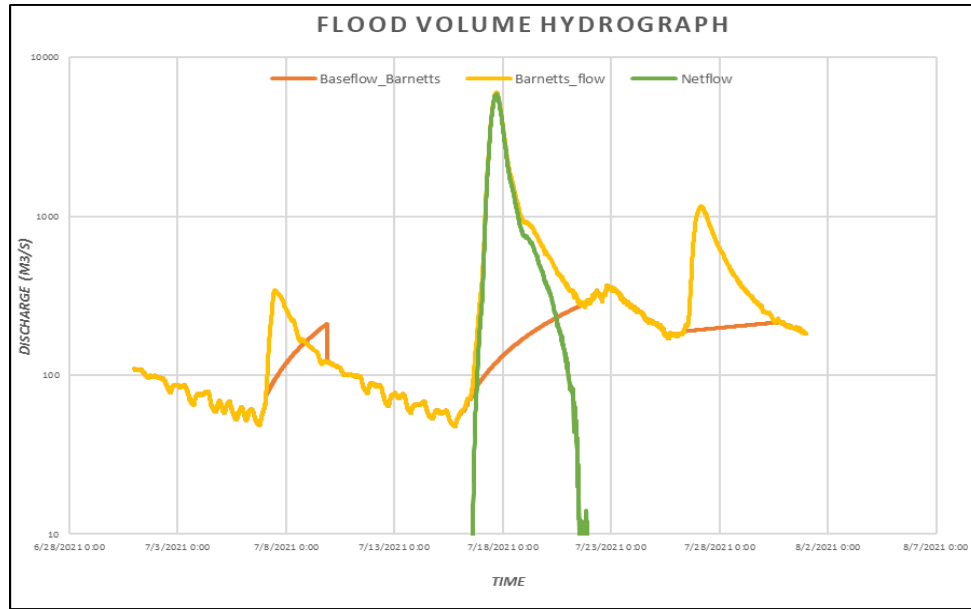
FLOOD VOLUME HYDROGRAPH

Figure 9: Flood volume hydrograph

4.2. Catchment precipitation

The selected interpolation methods from the geostatistical methods gave different results. The results varied, with RBK having the highest maximum precipitation value of 395.93 mm and the lowest minimum value of 53.82 mm. NN and RBF closely gave an expected spatial structural map, with high precipitation at highly elevated areas.

However, the NN area does not cover the entire catchment. Within the catchment, NN, RBF, and EBK replicate high precipitation at Onamalutu at Bartletts Creek Saddle, Onamalutu at Hilltop, Mt. Morris, and Top Valley when compared to the observed. IDW gave a poor spatial map of the areal catchment precipitation. The average catchment precipitation of each model was computed (Table 2) and compared with the average areal precipitation from the flood volume estimates. The RADAR rainfall sums (Figure 10) have the highest precipitation value at 506.45 mm with an average of 115.17 mm.

The yellow dots represent the rainfall stations, while the orange dot is the Blenheim station at MDC for orientation. NN and IDW evaluate the highest and lowest average catchment precipitation at 189.05 mm and 169.88 mm respectively. All four models overestimate the average

catchment precipitation when compared to the calculated areal average precipitation of the flood volume.

When compared with the rain RADAR data, the four models underestimate the maximum precipitation value.
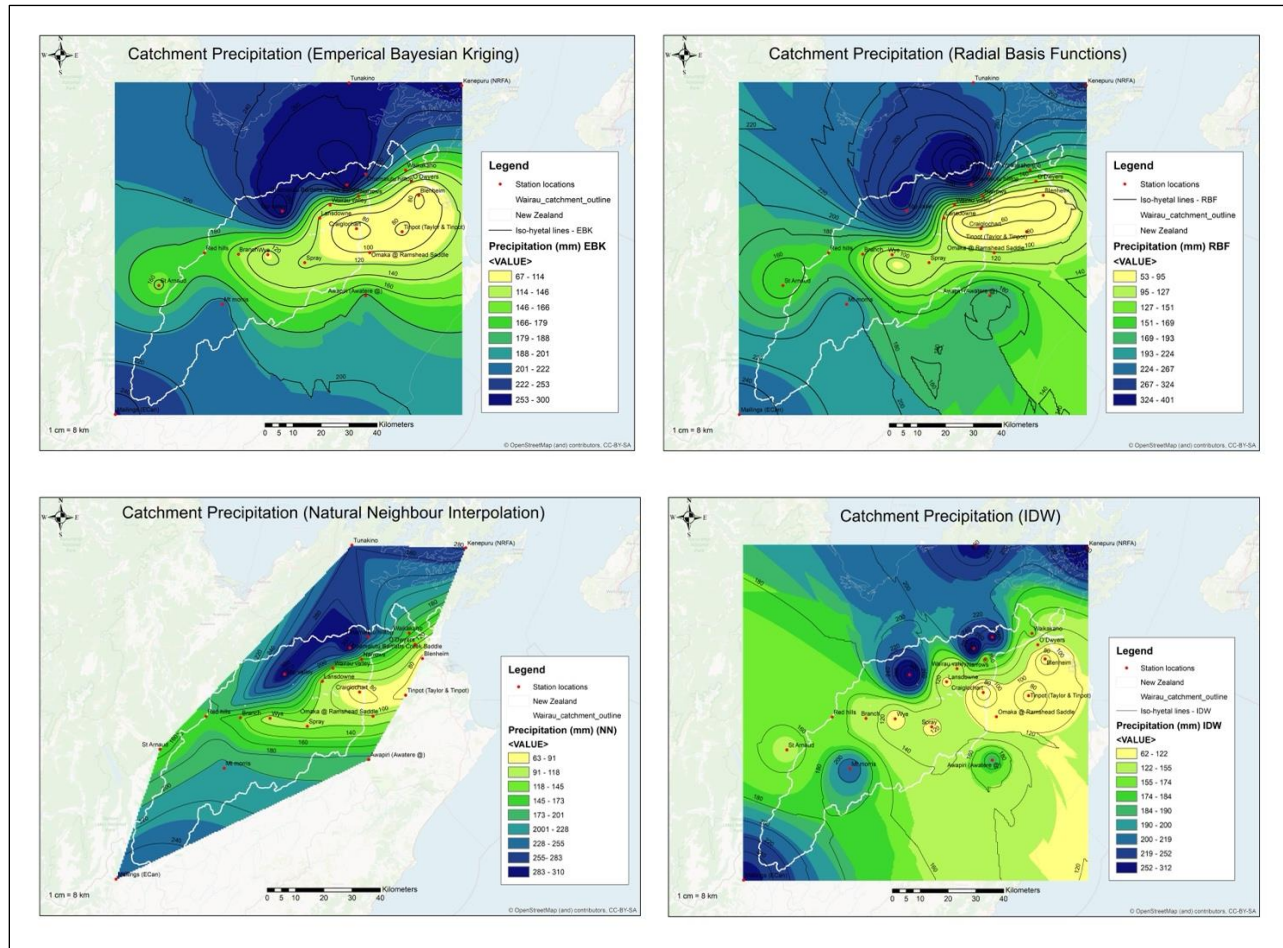
Figure 10: Geostatistical interpolations for IDW, EBK, RBF, and NN.
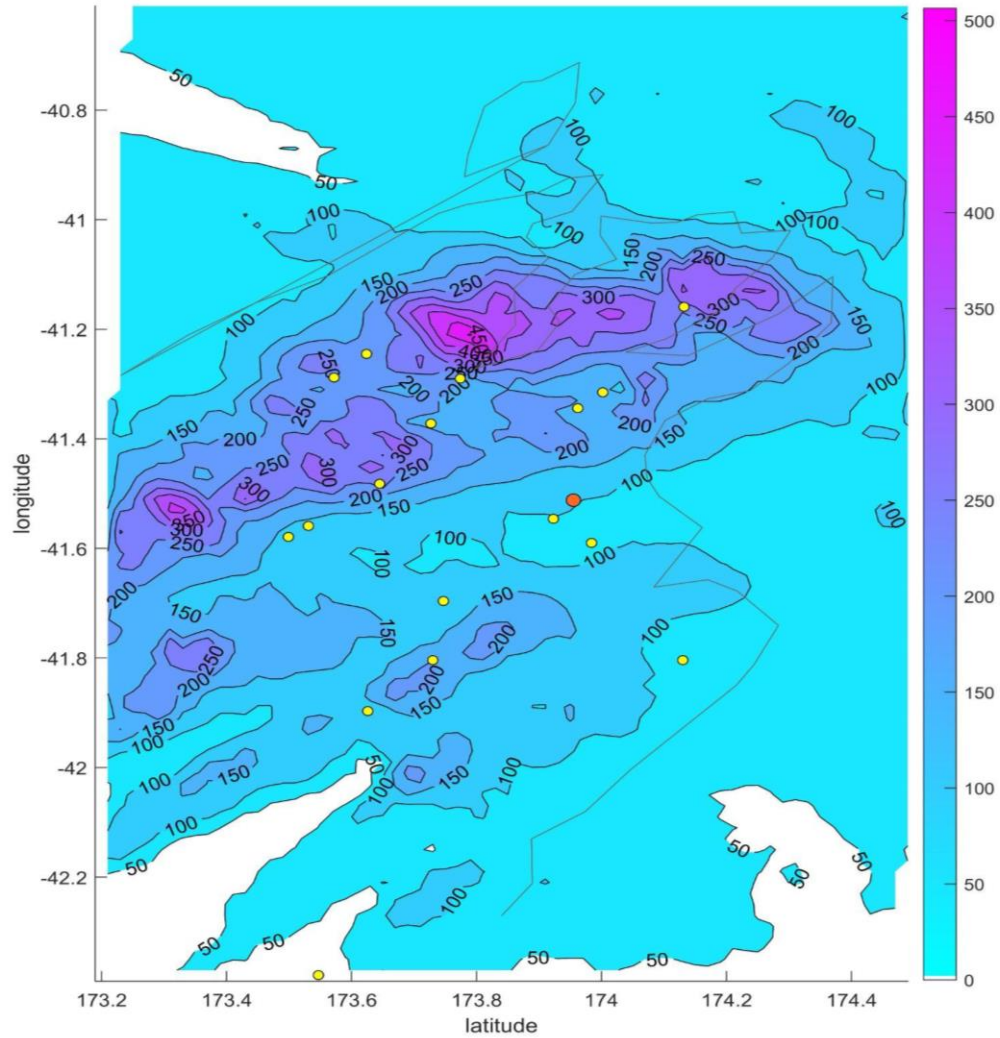
Figure 11: Aggregated rainfall data (RADAR) from 16th - 20th July 2021.

4.3. Ordinary kriging

Similarly, with the geostatistical interpolation schemes, the areal average precipitation of each model was evaluated using ordinary kriging interpolation. The exponential and spherical model types have varied width sizes of 1000 m and 2000 m. The exponential model at 1000 m and 2000 m gives similar spatial structural maps with a close average catchment precipitation value. The same result applies to the spherical model at 1000 m and 2000 m width sizes, as it gives similar spatial structural maps and similar average catchment precipitation.
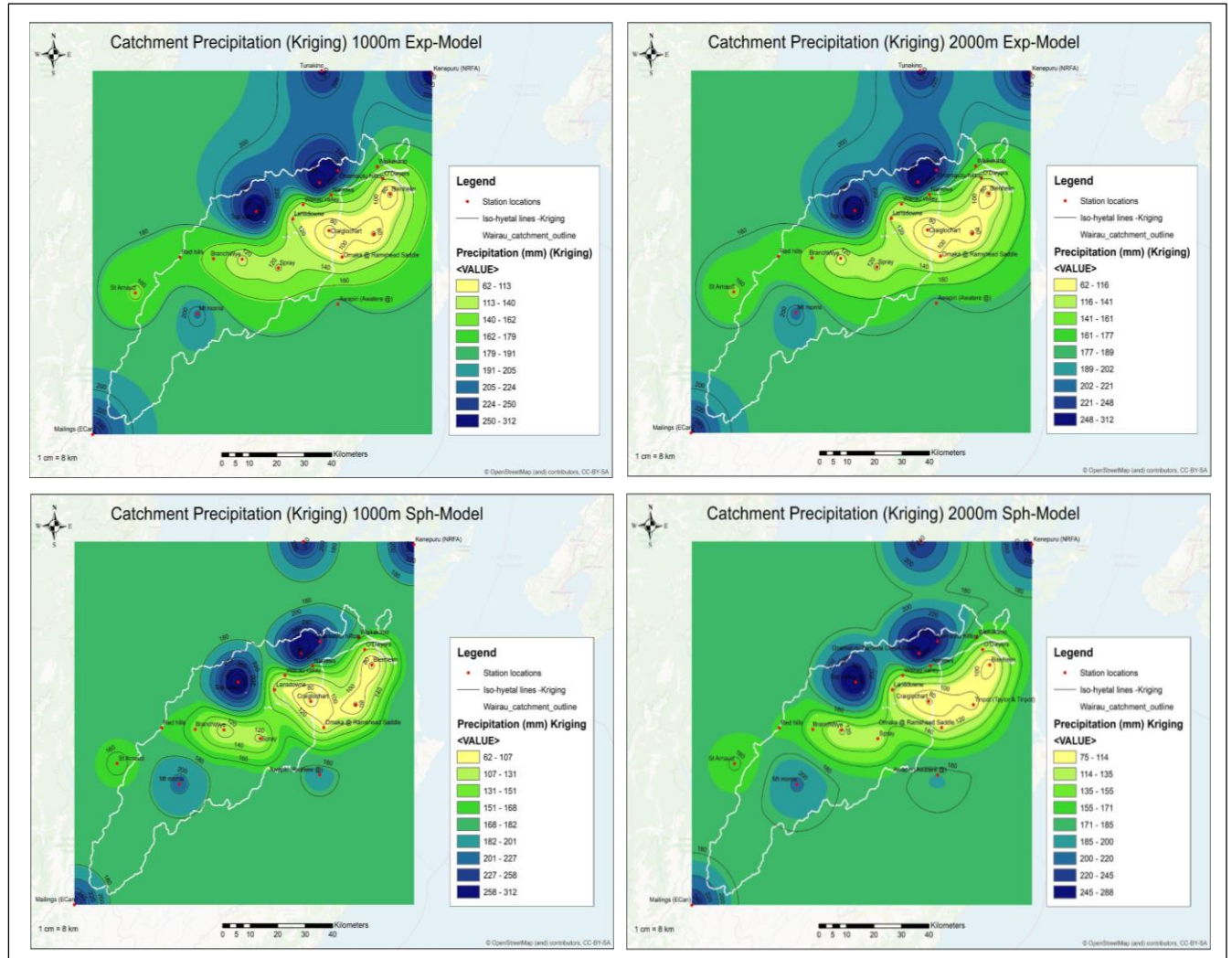
Figure 12: Exponential and Spherical models with varied width sizes of 1000 m and 2000 m.

However, the auto-kriging experimental variogram and the fitted variogram for exponential and spherical models are quite distinct. The spherical auto-kriging model underestimates the precipitation data, having the maximum precipitation value at 268.00 mm and minimum at 84.26 mm. The auto-kriging exponential model appears to have the highest average catchment precipitation value when compared with other models with varied width sizes. With a high standard deviation of the auto-kriging models, spherical and exponential, it implies that there is a high variance in the precipitation data.
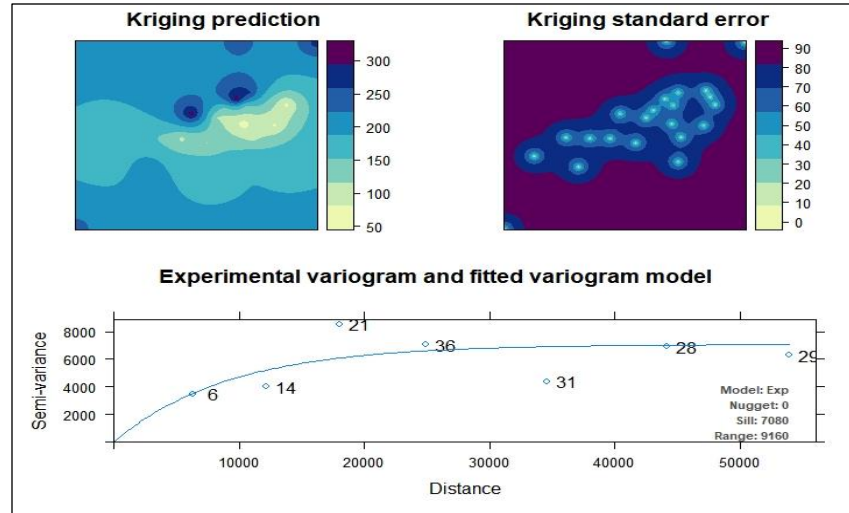
Figure 13: Auto-kriging for exponential model.
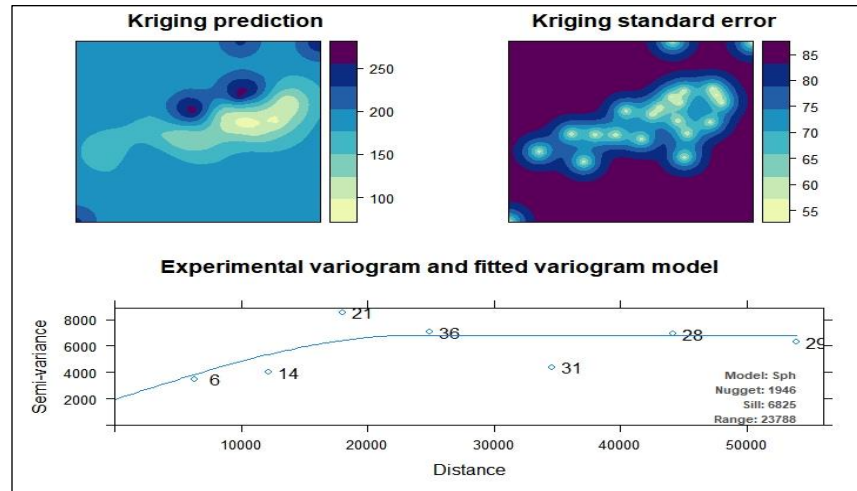
Figure 14: Auto-kriging for spherical model.

4.4. Runoff Coefficient

The runoff coefficient (C) is the volume of water superficially drained during rainfall to the total volume of precipitation during a given period (Bedient et al., 2013; Jnior, 2015). Evaporation and partial infiltration of collecting surfaces reduce runoff volume in wet weather, for which the infiltration rate is a determinant of the surface type. Similarly, the runoff coefficient is a collection surface-dependent factor that multiplies the accumulated rainfall to calculate the actual rainfall-runoff introduced into the catchment system.

Alternatively, the runoff coefficient is the factor used to calculate the effective impermeable area, which varies depending on the type of surface. Precipitation is one of the central factors when

evaluating and calculating the runoff coefficient, which may refer to isolated rainfall or a time interval in which high precipitation occurs (Júnior, 2015; Campos & Machado, 2018). The initial losses and infiltration capacity are met as precipitation increases. As a result, there would be an increase in runoff, resulting in a higher runoff coefficient (Tucci, 2000). There are relatively high runoff coefficients exhibited by the models. IDW has the highest C while NN has the lowest.

Table 2: Average catchment precipitation and runoff coefficient of each model

	MIN (mm)	MAX (mm)	MEAN (mm)	STD	Average Areal Precipitation (mm)	Runoff Coefficient
RAIN RADAR OBSERVED						
	62.00	506.45	115.17	78.82	148.68	0.77
INTERPOLATION MODELS						
NN	63.46	310.54	189.05	50.25	148.68	0.79
IDW	62.22	311.80	169.88	37.42	148.68	0.88
RBK	53.82	395.93	182.67	62.76	148.68	0.81
RBF	66.59	300.86	178.98	46.00	148.68	0.83
ORDINARY KRIGING						
Exp-Model 1000m	62.22	311.83	176.16	35.87	148.68	0.84
Exp-Model 2000m	62.26	311.82	175.48	33.48	148.68	0.85
Sph-Model 1000m	62.15	311.80	173.12	35.05	148.68	0.86
Sph-Model 2000m	75.21	288.10	174.53	32.67	148.68	0.85

AUTO-KRIGING						
Exp	62.10	311.84	183.12	80.23	148.68	0.81
Sph	84.26	268.00	178.54	80.73	148.68	0.83

4.5. Groundwater analysis

The stage plot of all the wells considered in the study is presented in figure 14. The water table started to rise on July 16 at 18:00 and reached the peak on July 17 at 13:00. 4 hours later the flood reached the Barnetts station situated downstream to the study site. It is shown that the table increased with the flood and decreased simultaneously. The temperature change in the water table during the flood event is also shown in the figure below. The lag response of the parameters of the water table with the flood event is further studied in this research.
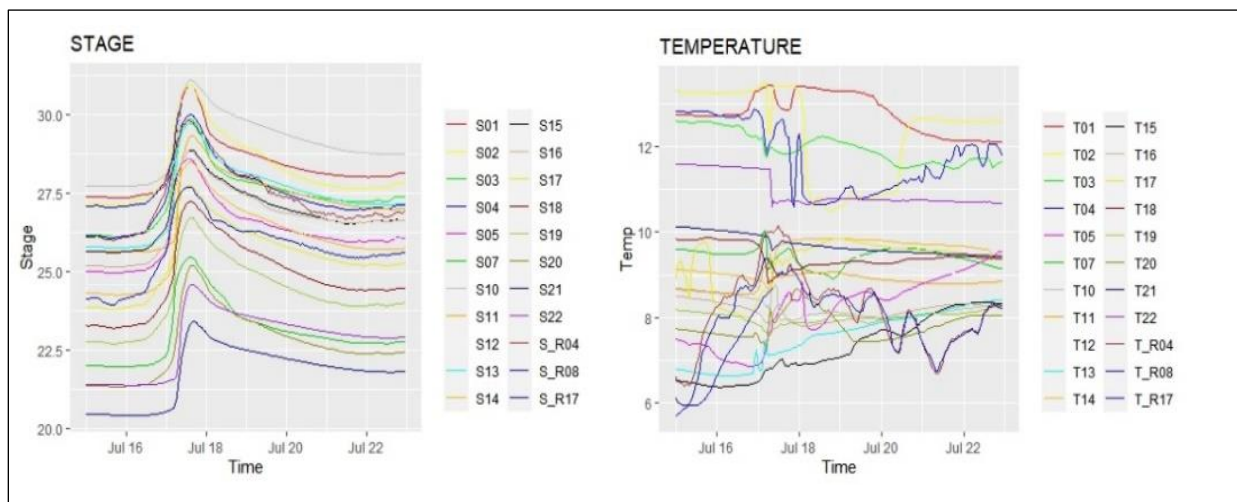

Figure 15: Plot of the parameters of the monitoring wells during the flood event.

4.5.1 Generation of contour maps

The measuring wells at the study site have three wells along the river and the rest at the groundwater table. The contour maps are derived using both piezometric head and temperature. The river flows from the southwest to the northeast direction. The maps are derived for certain time periods at the study site to relate the maps with the flood event. The start of the flood event on July 16 at 18:00 is shown in the figure below. The plot next to the contour maps represents the flood hydrograph at Barnetts station and the red dot indicates the time period of the contour maps in the flood event.
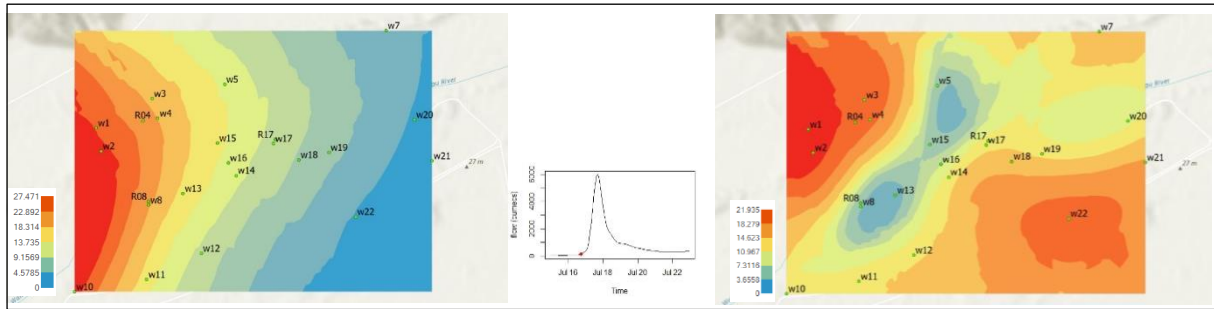
Figure 16: Contour maps of piezometric head and temperature on July 16 at 18:00

The decrease in the head of the water level from the west to the east direction can be seen from figure 15 above. The flow of the groundwater on a larger scale could be seen in the same direction as the flow of the river. The temperature is low in the wells closer to the river flow region. The water flowing regions are with lesser temperatures than the other surrounding regions. As the flood progresses and reaches the peak on July 17 at 13:00, the groundwater shifts and that could be seen in figure 16.
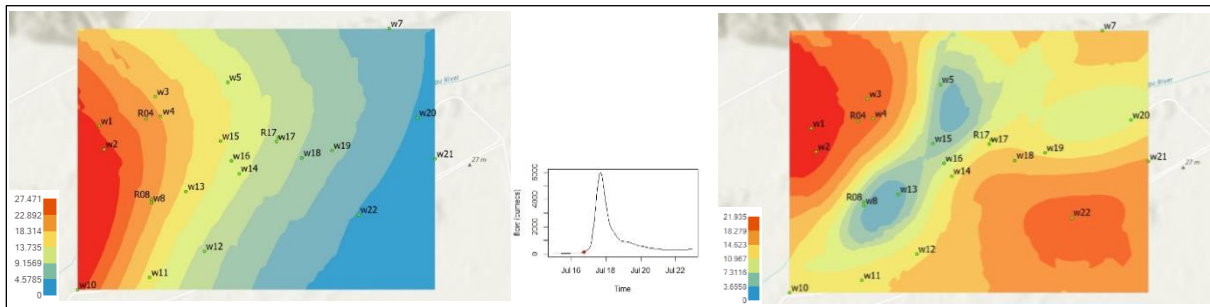
Figure 17: Contour maps of piezometric head and temperature on July 17 at 13:00

A surge in the piezometric head is visible through the study site during the time period. The north-western part and western part of the study site had the infiltrated flood which gave into the rise of the aquifers. The temperature contour maps show the spread of decrease in temperature during the peak in the north-western part of the study site and developed a further decrease in river path close to stations 19 and 20. And during the peak of the flood hydrograph, the contour map shows a shift of water level change in the northern part of the study site.

Figure 18: Contour maps of piezometric head and temperature on July 17 at 17:00

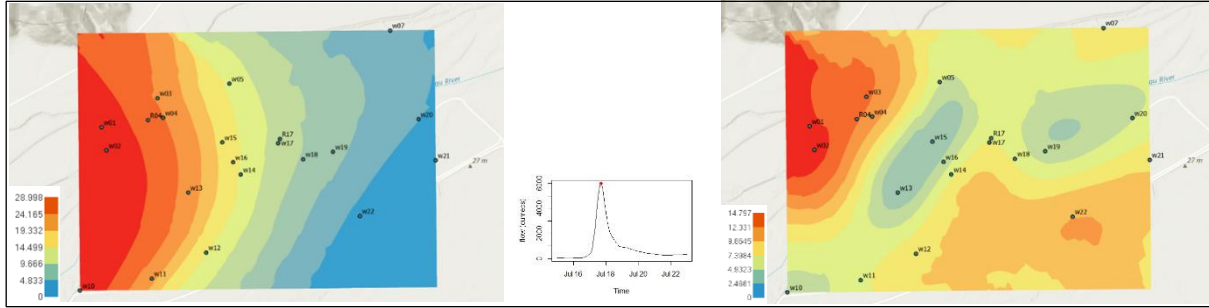As the figure 17 denote the infiltration of water into the aquifers, the process of the groundwater rise happens fast and could mean the shallow depth of aquifers.
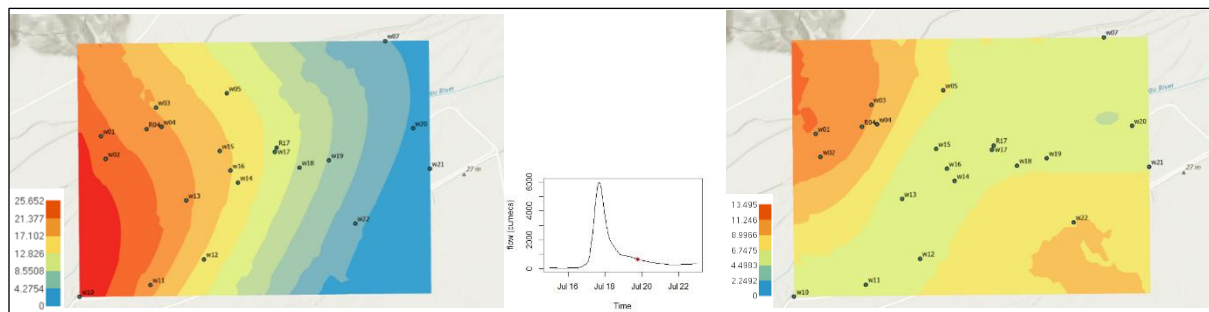
Figure 19: Contour maps of piezometric head and temperature on July 19 at 18:00

And two days after the flood event, the water table reduces in this contour map above. Also, there is an increase in temperature along with the river flow. This could mean the faster discharge into the stream as the hydrograph shows the higher flow of water when compared with the flow before the flood event.

4.5.2. Difference maps

The contour maps are produced as difference maps with one map as stationary map and here it is from the time, July 15, 08 hours. The generated contour maps below are for the stationary period considered.
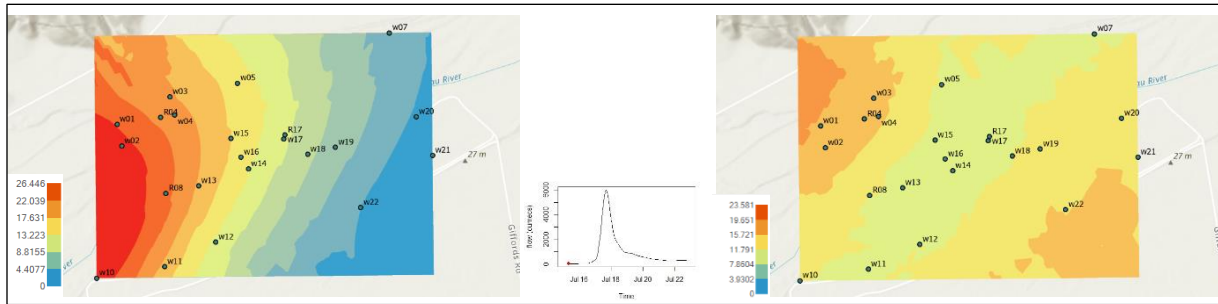
Figure 20: Difference Contour maps of piezometric head and temperature on July 15 at 08 hours

The changes between contour maps are better enhanced in the difference maps. The difference during flood ought to be positive as there is an increase in water table but the temperature drops than before and that specific difference through certain regions could be seen. But the temperature contour maps here are inverted showing positive values instead of negative ones. This could mean the difference maps are absolute difference contour maps.

Figure 21: Difference Contour maps of piezometric head and temperature on July 16 at 18 hours

The higher difference in the north-western part shows the increased movement of groundwater in that region.
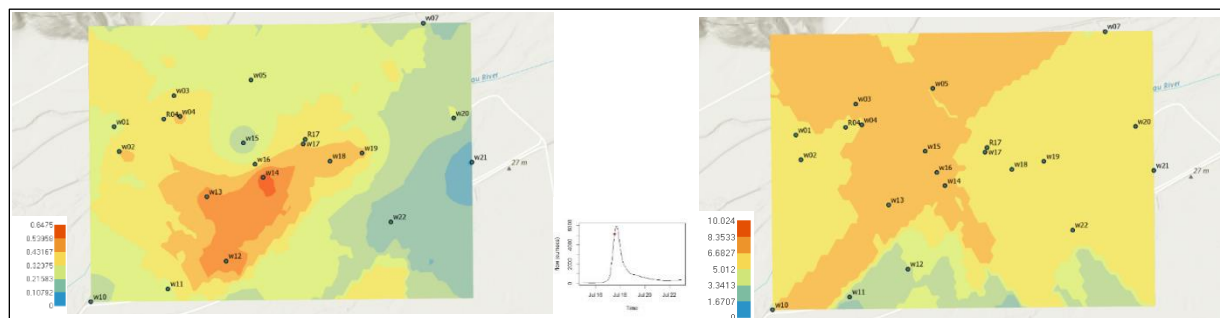
Figure 22: Difference Contour maps of piezometric head and temperature on July 17 at 13 hours

As the peak is closer, the difference in water level is highest at the river path than the northwestern region. Also, there is a similar change in the temperature contour map.
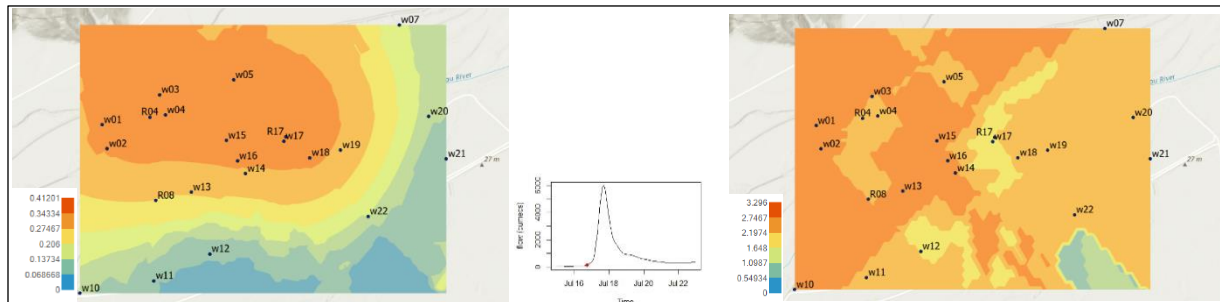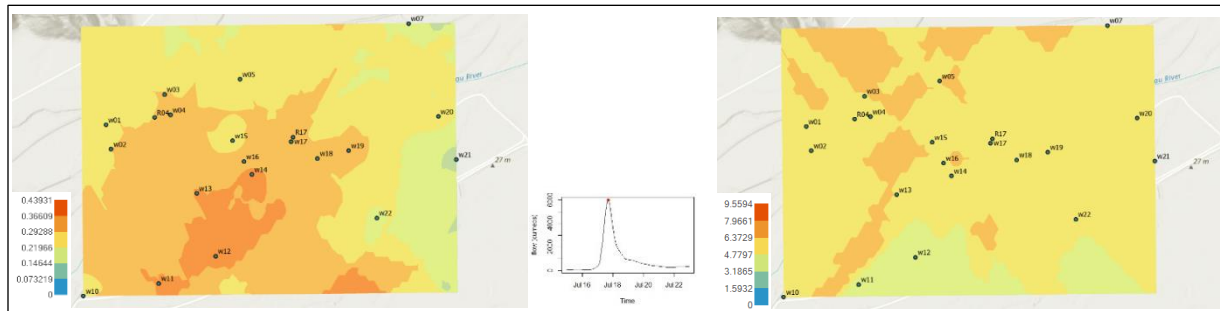

Figure 23: Difference Contour maps of piezometric head and temperature on July 17 at 17 hours

During the peak, the increase in water level is seen surrounding the river path and especially close to stations 11, 12 and 13. The temperature shows an evenly spread change of temperature and a small part of the region has an increased drop. Then the difference maps two days after the flood are generated.

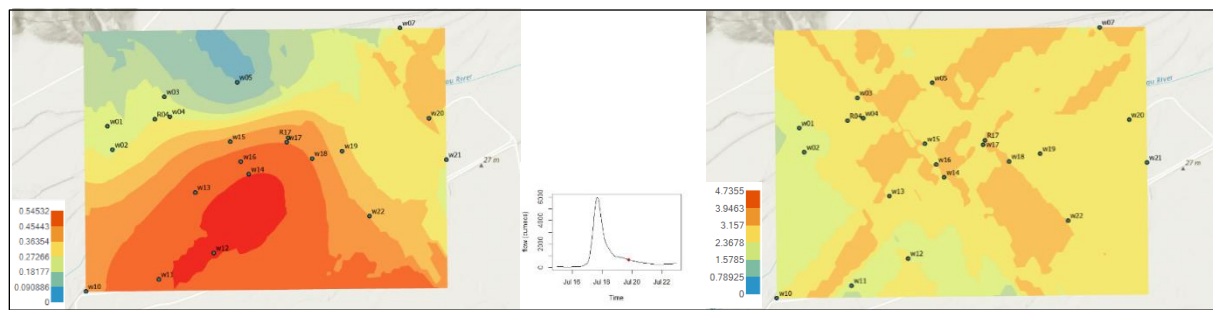*Figure 24: Difference Contour maps of piezometric head and temperature on July 19 at 18 hours*

Though the flood hydrograph shows the end of the flood event, the flow is higher than the base flow, and the contour map shows a difference in the southwest region. The higher difference in certain regions closer to certain wells could be a case to investigate further for connectivity of aquifers to the river.

4.6 Time lag analysis

4.6.1 Cross-correlation of temperature of river stage with wells

The temperature of each groundwater borewell and its accompanying river stage were cross-correlated. This comparison was made to better understand how each well responded to the river's temperature indication. The aquifer is thought to be refilled by the river. As shown in figure 24, The correlation coefficient was obtained for each displacement (i.e., the correlation coefficient function was computed for each shift). The x-axis (lag) depicts the lag duration, while the y-axis (ACF) depicts the correlation value. The correlation with a 100-unit x-axis spacing and a 0.2-unit y-axis spacing. The 95 percent confidence interval is represented by the blue break lines in the figure's centre. The plots are divided into three types, which will be addressed in the Wells categorization.

Category 1
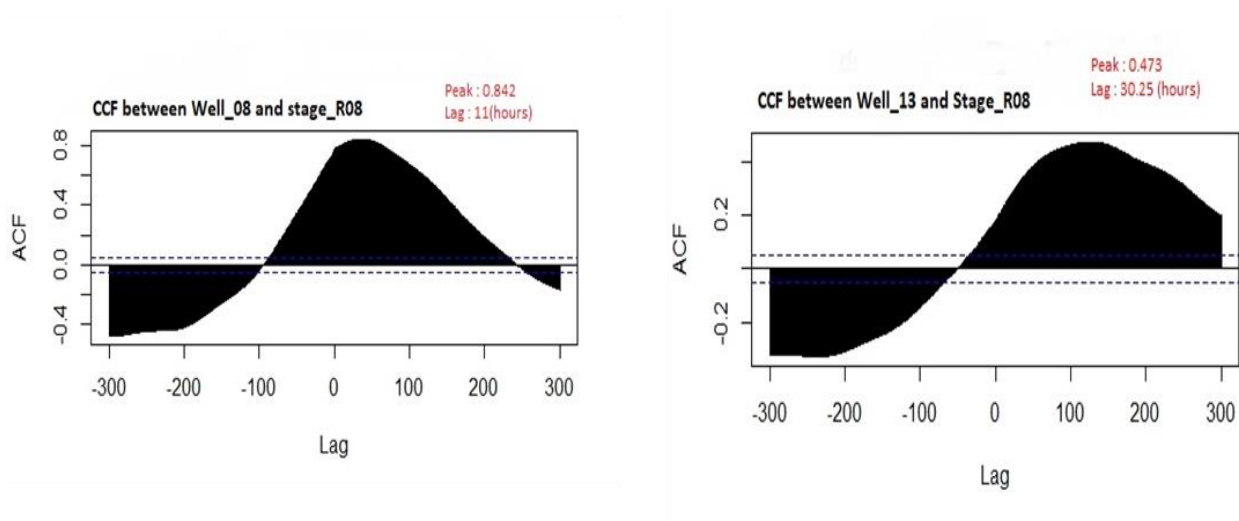
Figure 25: Cross correlation plots of the groundwater borewells W08 and W13 and Head R08.

Figure 24 shows the cross-correlation plots of groundwater borewells. The steep state begins to increase from-100 lag (negative lag) and reaches its maximum at 0.842 with a travel time of 11 hours, indicating a good correlation. The cross-correlation function (CCF) comparison of the Well_ W08 and stage_R08 showed less temporal variability as the steep stated to increase from -100 lag (negative lag) and reaches its maximum at 0.842 with a travel time of 11 hours, indicating a good correlation.

The CCF was estimated in the same way for Well W13 and Stage W08, yielding a lag distance of 30.25 hours and a maximum peak of 0.473. In addition, when compared to the well 13 with river stage 08, the well 08 has showed a high significant reaction. The shorter distance between the stage and the ground borewell may have resulted in this high association.

Category 2
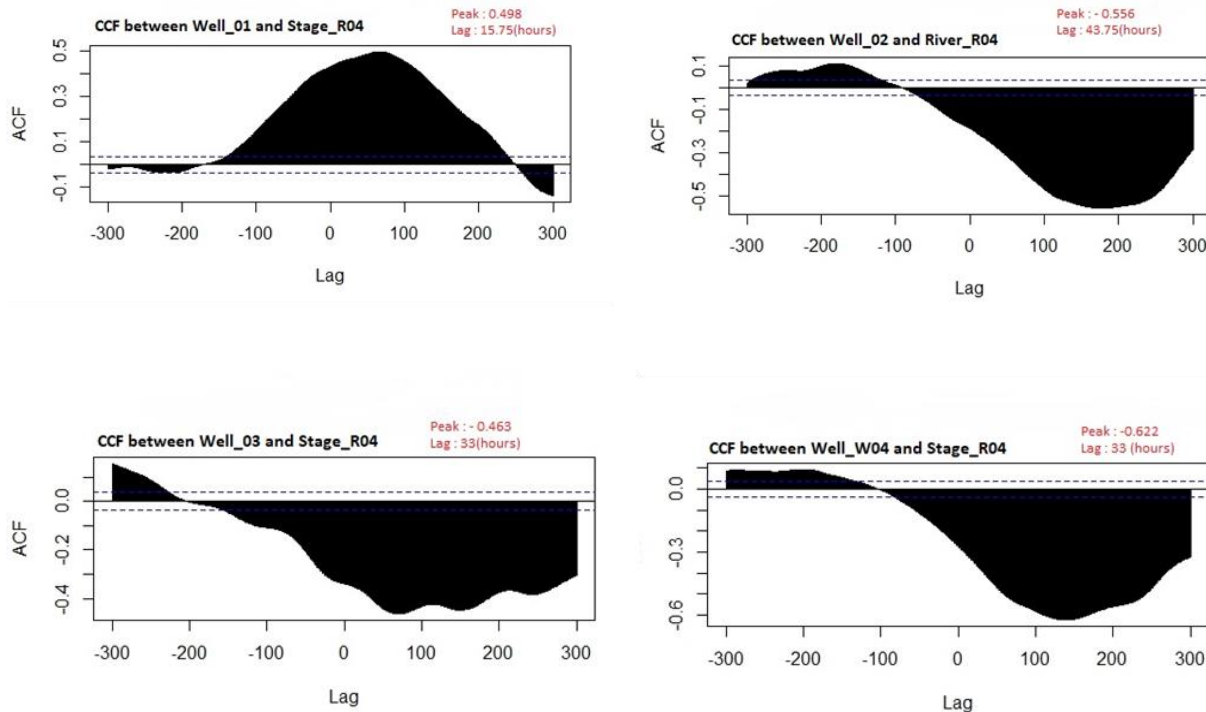
Figure 26: CCF plots of wells W01, W02, W03, W04 and stage_ R04.

Figure 25 represents the cross-correlation function plots head_R04 and their corresponding groundwater borewells (W01, W02, W03, W04).

The CCF for the well_W01 shows the shift (displacement) starting at –150 and reaches the maximum correlation at 0.498 with a lag distance of 15.75 hours. The temperature correlation of groundwater well_W02 indicates a sudden drop at lag -100 and peaks it maximum the correlation value at -0.556 with a travel distance of 43.75 hours. Similarly, the well_W03 and well_W04

showed a negative correlation with its max. peak at -0.463 and -0.622 respectively. Both the wells W03 and W04 resulted a lag distance of 33 hours which proves that the travel time to both these stations are same.

Category 3
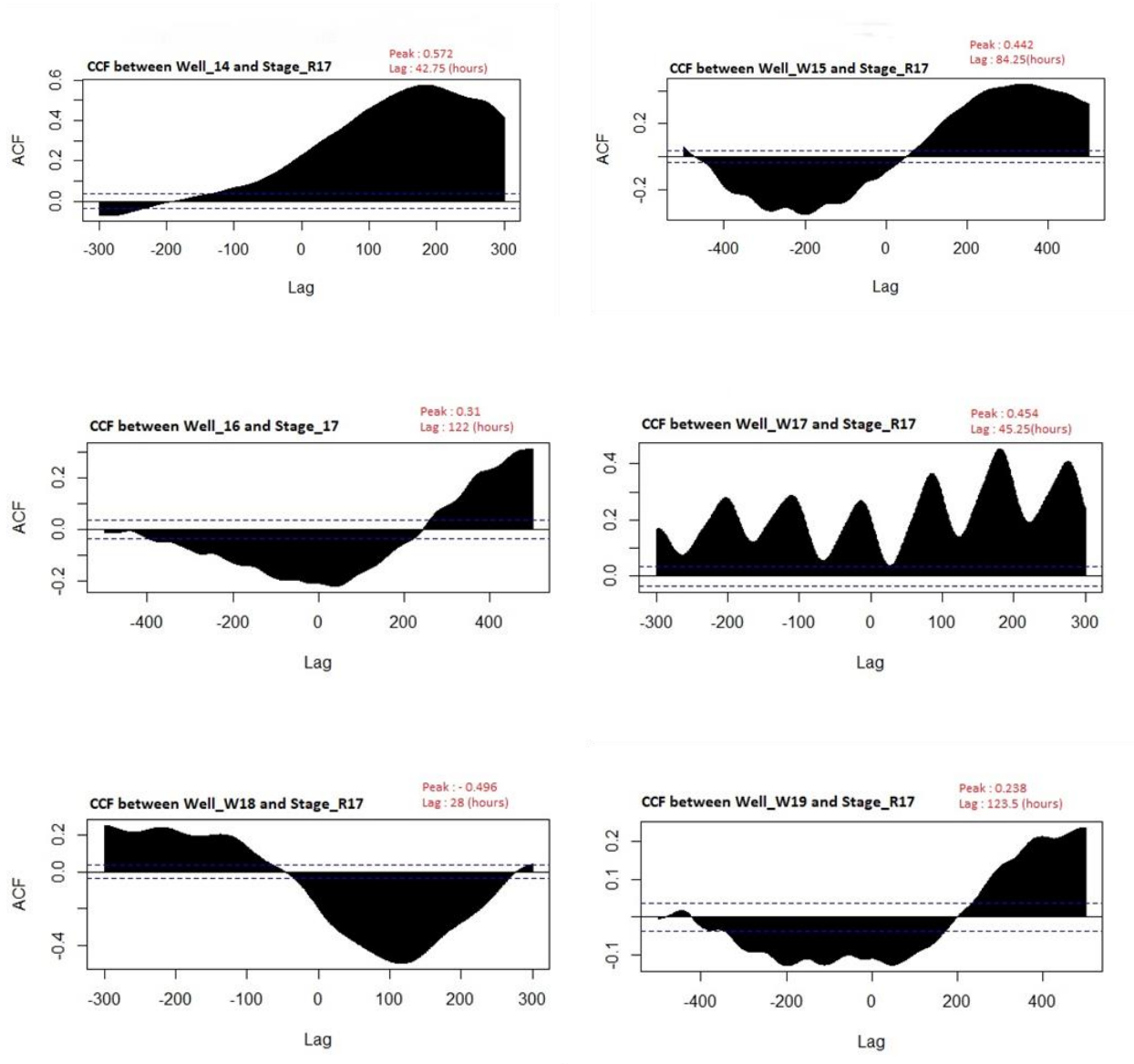
Figure 27: CCF plots of well_w14, W15, W16, W17, W18, W19, and stage_R17.

The Figure 26 shows the cross-correlation plots Stage_R17 and their corresponding groundwater wells (W14, W15, W16, W17, W18, W19)

The highest correlation was seen in the CCF plots for well W14 and W 17, with the shift in lag at – 200, peaking at 0.572 and a lag distance of 42.75 hours for well W14, and at 0.454 and a lag duration of 45.25 hours for well W17. This significant correlation could be due to the short distance between the two points and the geomorphological circumstances.

Similarly, the CCF for W15 and W16 showed a positive lag with peaks at 0.442 and 0.31, respectively, with lag times of 84.25 hours and 122 hours. With least peak values of 0.496 and 0.238 and lag times of 28 hours and 123.5 hours, wells W18 and W19 showed a substantial temporal variation.

4.6.2. Zone classification based on cross-correlation

The wells in the study region are divided into groups based on the time lag between the temperature of the wells and the river stage. The zoning of wells into three categories is depicted in Figure 27 based on the delayed responses of each well.
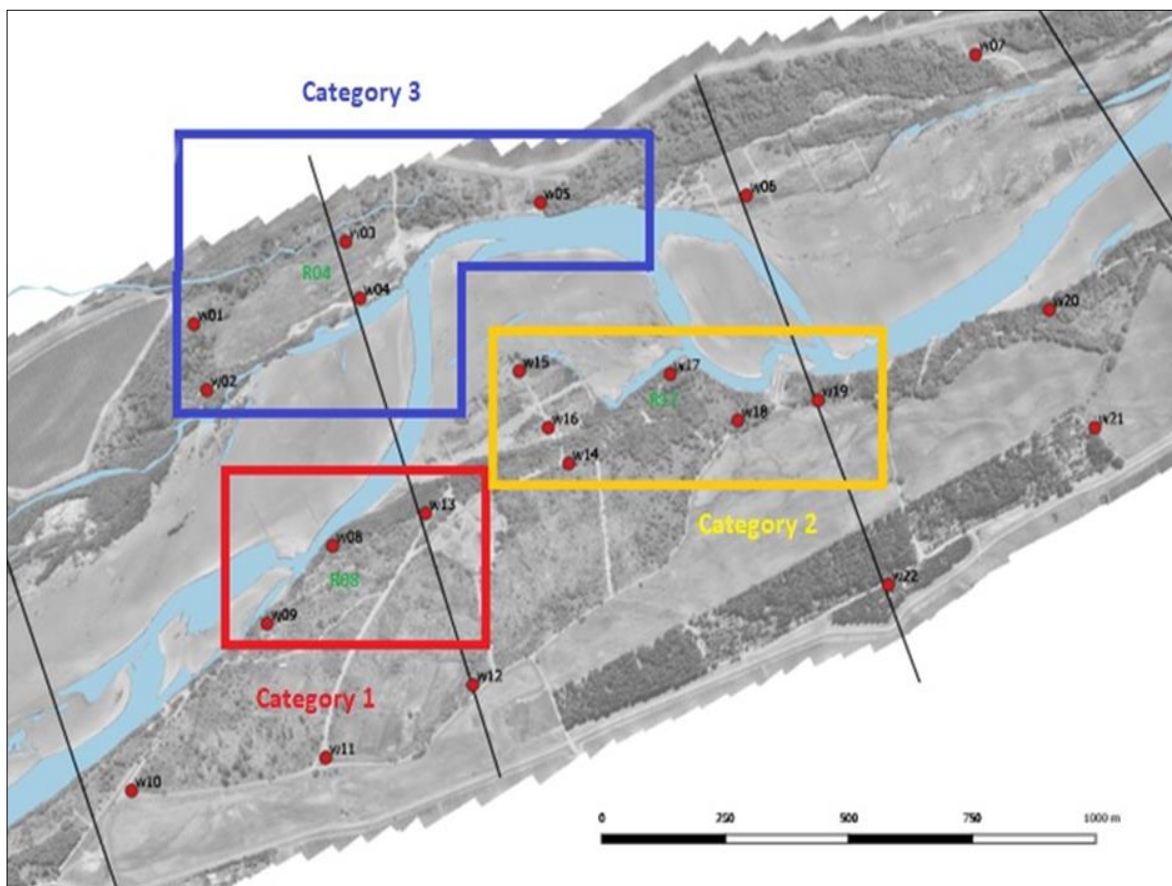
Figure 28: Categorisation of zones according to lag responses.

The lag responses of wells in relation to their corresponding zones are shown in Table 3.

Table 3: Cross- correlation and Lag values for different stations.

	Temperature		
Station	**Correlation value**	**Lag**	**lag (in hrs.)**
W01 & R04 (groundwater 01 & River 4)	0.498	63	15.75
W02 & R04 (groundwater 02 & River 4)	-0.556	174	43.5
W03 & R04 (groundwater 03 & River 4)	-0.463	67	16.75
W04 & R04(groundwater 04 & River 4)	-0.622	132	33
W08 & R08 (groundwater 08 & River 8)	0.842	44	11
W13 & R08(groundwater 13 & River 8)	0.473	121	30.25
W14 & R17 (groundwater 14 & River 17)	0.572	171	42.75
W15 & R17 (groundwater 15 & River 17)	0.442	337	84.25
W16 & R17 (groundwater 16 & River 17)	0.31	488	122
W17 & R17 (groundwater 17 & River 17)	0.454	181	45.25
W18 & R17 (groundwater 18 & River 17)	-0.496	112	28

W19 & R17 (groundwater 19 & River 17)	0.238	494	123.5

The category 1 (i.e., wells reacting to stage R08) showed a significant temporal variation, as both wells had positive lag values with the shortest lag time, indicating that the category 1 had a strong correlation with short lag time. Table 3 shows that wells reacting to stage R17, category 2 had a longer travel time with a lag range of 28 to 123.5 hours, indicating that category 2 had an increasing lag time with less correlation. In contrast, group 3 had a very low correlation with lags in an unknown range and exhibited no significant correlation.

5. Discussions

It can be deduced that the varied width sizes for exponential and spherical models do not distinctly affect the output of the areal average catchment precipitation. This might be a result of the uncertainties in the chosen variogram. It is evident that the spherical autofit model is not suitable for areal catchment precipitation in this study area. The sensitivity of the interpolation methods were quiet observable as we could see their variations in the spatial maps

There was a surcharge in the streamflow a few days before the main flood event. This could have made the soil strata to be already saturated with the infiltrated water. This incident gives the expectation of a higher run-off coefficient. This also makes the flood event to be a flash flood.

There is an immediate response to the groundwater level increase, especially in the north-western part of the study site. This could be a result of the existence of discharge points downstream and the simultaneous decrease in groundwater through the gaining stream. Shallow aquifers might immediately respond to the changes in temperature where the fast increase in temperature after the flood event is noticed in the contour maps of temperature.

The contour maps give confirmation of the correlation of the monitoring wells closer to the river have taken lesser lag time. The negative correlation of the wells could possibly mean that the surface- groundwater near to those stages could be weak. The time lag response proved that the zones which are lying far from the river stages have higher lag response which proves infiltration of water highly depends on the distance.

References

1. Bennett, B., Leonard, M., Deng, Y. and Westra, S., 2018. An empirical investigation into the effect of antecedent precipitation on flood volume. *Journal of Hydrology*, 567, pp.435-445.

2. Bosch, D., Arnold, J., Allen, P., Lim, K. and Park, Y., 2017. Temporal variations in baseflow for the Little River experimental watershed in South Georgia, USA. *Journal of Hydrology: Regional Studies*, 10, pp.110-121.

3. Brown, L., 1981. Late Quaternary geology of the Wairau Plain, Marlborough, New Zealand. *New Zealand Journal of Geology and Geophysics*, 24(4), pp.477-485.

4. Bui, M., Lu, J. and Nie, L., 2020. Sensitivity analysis of the SWAT model to spatial distribution of precipitation in streamflow simulation in an Arctic watershed. *IOP Conference Series: Earth and Environmental Science*, 581(1), p.012025.

5. Calculation of Uncertainty in the Variogram by Julián M. Ortiz Clayton Deutsch Clayton Deutsch, 2002 (page 1 - 9)

6. Cardoso, T., Machado, R. and Mortene, M., 2019. Determination of the runoff coefficient (C) in catchments based on analysis of precipitation and flow events.

7. Chae, G., Yun, S., Kim, D., Kim, K. and Joo, Y., 2010. Time-series analysis of three years of groundwater level data (Seoul, South Korea) to characterize urban groundwater recharge. *Quarterly Journal of Engineering Geology and Hydrogeology*, 43(1), pp.119 - 120.

8. Chappell, P. (2016). The climate and weather of Marlborough. *New Zealand Meteorological Service Miscellaneous Publication, 115* (12)

9. Christensen, K. and Doscher, C. (2010). The interaction of river engineering and geomorphology in the Lower Wairau River, Marlborough, New Zealand. *Journal of Hydrology (NZ), 49*(2), 79-98. http://hydrologynz.co.nz/downloads/20110420-023728-JOHNZ_v49_2_Christensen.pdf

10. Cookson, C. (2020). Wairau River. Retrieved from https://www.marlboroughonline.co.nz/marlborough/information/geography/rivers/wairau -river/

11. Goel, M., 2011. Runoff Coefficient. *Encyclopedia of Earth Sciences Series*, pp.952-953.

12. Goovaerts, P., 2010. Combining Areal and Point Data in Geostatistical Interpolation: Applications to Soil Science and Medical Geography. *Mathematical Geosciences*, 42(5), pp.535-554.

13. Gringarten, E. and Deutsch, C.V., 2001. Teacher's aide variogram interpretation and modeling. Mathematical Geology, 33(4), pp.507-534.

14. Hadi, S. and Tombul, M., 2018. Comparison of Spatial Interpolation Methods of Precipitation and Temperature Using Multiple Integration Periods. *Journal of the Indian Society of Remote Sensing*, 46(7), pp.1187-1199.

15. Hervai, A., Farics, É., Sisák, I., Farkas, G., Kovács, J. and Lóczy, D., 2020. Influence of Flood Waves, Production Wells, and Precipitation on Shallow Groundwater Using a Linear Regression Model Approach Based on a Case Study of Mohács Island, Hungary. *Water*, 12(5), p.1359.

16. Julínek, T., Duchan, D. and Říha, J., 2020. Mapping of uplift hazard due to rising groundwater level during floods. *Journal of Flood Risk Management*, 13(4).

17. Kobayashi, S., Ota, Y., Harada, Y., Ebita, A., Moriya, M., Onoda, H., Onogi, K., Kamahori, H., Kobayashi, C., Endo, H., Miyaoka, K. And Takahashi, K., 2015. The Jra-55 Reanalysis: General Specifications And Basic Characteristics. *Journal Of The Meteorological Society Of Japan. Ser. Ii*, 93(1), Pp.5-48.

18. Korytny, L. And Kichigina, N., 2006. Geographical Analysis Of River Floods And Their Causes In Southern East Siberia. *Hydrological Sciences Journal*, 51(3), Pp.450-464.

19. Liu, Y., Gebremeskel, S., De Smedt, F., Hoffmann, L. and Pfister, L., 2003. A diffusive transport approach for flow routing in GIS-based flood modeling. *Journal of Hydrology*, 283(1-4), pp.91-106.

20. Marchant, B. and Lark, R., 2004. Estimating Variogram Uncertainty. *Mathematical Geology*, 36(8), pp.1-5.

21. Mondal, I., Bandyopadhyay, J. and Paul, A., 2016. Estimation of hydrodynamic pattern change of Ichamati River using HEC RAS model, West Bengal, India. *Modeling Earth Systems and Environment*, 2(3).

22. Morgenstern, U., Davidson, P., Townsend, D.B., White, P.A., Van Der Raaij, R.W., Stewart, M.K., Moreau, M., Daughney, C. (2019). From rain through river catchment to

aquifer: the flow of water through the Wairau hydrologic system. Lower Hutt (NZ): GNS Science. 83 p. (GNS Science report; 2019/63). doi:10.21420/7125-ST46.

23. Morris, S., Cobby, D., Zaidman, M. and Fisher, K., 2015. Modelling and mapping groundwater flooding at the ground surface in Chalk catchments. *Journal of Flood Risk Management*, 11, pp.S251-S268.

24. Mutreja, K. N., 1990. *Applied Hydrology*. New Delhi: Tata McGraw-Hill.

25. Ogras, S. and Onen, F., 2020. Flood Analysis with HEC-RAS: A Case Study of Tigris River. *Advances in Civil Engineering*, 2020, pp.1-13.

26. Ortiz, J. and Deutsch, C.V., 2002. Calculation of uncertainty in the variogram. Mathematical Geology, 34(2), pp.169-183.

27. Ortiz, J., 2012. Jef Caers: Modeling Uncertainty in the Earth Sciences. *Mathematical Geosciences*, 45(1), pp.79-86.

28. Posavec, K., Vukojević, P., Ratkaj, M. and Bedeniković, T., 2016. Cross-correlation modelling of surface water – groundwater interaction using the excel spreadsheet application. *Rudarsko-geološko-naftni zbornik*, 32(1), pp.5 - 7.

29. Subramanya, K., 1991. *Engineering Hydrology*. New Delhi: Tata McGraw-Hill

30. Variogram Interpretation and Modeling by Emmanuel Gringarten and Clayton V. Deutsch, 2001 (page 507 - 510)

31. Williman, E.B., 1995. Flood Frequency Analysis for the Wairau River, Marlborough. Journal of Hydrology (New Zealand), pp.71-93.

32. Wöhling, T., Wilson, S., Wadsworth, V. and Davidson, P., 2020. Detecting the cause of change using uncertain data: Natural and anthropogenic factors contributing to declining groundwater levels and flows of the Wairau Plain aquifer, New Zealand. Journal of Hydrology: Regional Studies, 31, p.100715.

33. Wu, C., Mossa, J., Mao, L. and Almulla, M., 2019. Comparison of different spatial interpolation methods for historical hydrographic data of the lowermost Mississippi River. *Annals of GIS*, 25(2), pp.133-151.

34. Yang, R. and Xing, B., 2021. A Comparison of the Performance of Different Interpolation Methods in Replicating Rainfall Magnitudes under Different Climatic Conditions in Chongqing Province (China). *Atmosphere*, 12(10), p.1318.

35. Zeiger, S. and Hubbart, J., 2017. An Assessment of Mean Areal Precipitation Methods on Simulated Stream Flow: A SWAT Model Performance Assessment. *Water*, 9(7), p.459.

36. Ziegel, E., Deutsch, C. and Journel, A., 1998. Geostatistical Software Library and User's Guide. Technometrics, 40(4), p.357.

37. 2011. *Heat as a tracer for groundwater-surface water interaction*. PhD. Vrijie Universitiet Brussel.

38. 2015. *Wairau River-Wairau Aquifer Interaction*. Christchurch: Lincoln Agritech Limited, pp.6 - 9.